Cathodic Zn Underpotential Deposition: An Evitable Degradation Mechanism in Aqueous Zinc-Ion Battery

Shaohua Zhu [a,1], Yuhang Dai [a,c,d,1], Jinghao Li [a,1], Chumei Ye [f], Wanhai Zhou [b], Ruohan Yu [a], Xiaobin Liao [e], Jiantao Li [a], Wei Zhang [c], Wei Zong [c], Ruwei Chen [c], Guanjie He [c,d,*], Dongliang Chao [b,*], Qinyou An [a,*]

[a.] *State Key Laboratory of Advanced Technology for Materials Synthesis and Processing, Wuhan University of Technology, Wuhan 430070, China.*

[b.] *Laboratory of Advanced Materials, Shanghai Key Laboratory of Molecular Catalysis and Innovative Materials, and School of Chemistry and Materials, Fudan University, Shanghai 200433, P. R. China*.

[c.] *Christopher Ingold Laboratory, Department of Chemistry, University College London, 20 Gordon Street, London WC1H 0AJ, U.K.*

[d.] *Electrochemical Innovation Lab, Department of Chemical Engineering, University College London, London WC1E 7JE, U.K.*

[e.] *State Key Laboratory of Silicate Materials for Architectures, Wuhan University of Technology, Wuhan 430070, China*

[f.] *Department of Materials Science and Metallurgy, University of Cambridge, Cambridge CB3 0FS, U.K.*

[1] *These authors contributed equally to this work.*

* *Corresponding authors.*

E-mail addresses: anqinyou86@whut.edu.cn (Q. An), chaod@fudan.edu.cn (D. Chao), g.he@ucl.ac.uk (G. He)

Abstract

Aqueous zinc-ion batteries (AZIBs) are promising for large-scale energy storage, but their development is plagued by inadequate cycle life. Here, for the first time, we reveal an unusual phenomenon of cathodic underpotential deposition (UPD) of Zn, which is highly irreversible and regarded as the origin of the inferior cycling stability of AZIBs. Combining experimental and theoretical simulation approaches, we propose that the UPD process accords with a two-dimensional nucleation and growth model, following a thermodynamically feasible mechanism. Furthermore, the universality of Zn UPD is identified in systems, including VO_2//Zn, TiO_2//Zn, and SnO_2//Zn. In practice, we propose and successfully implement the removal of cathodic Zn UPD and significantly mitigate the degradation of the battery by controlling the end-of-discharge voltage. This work provides new insights into the degradation of AZIBs and brings the cathodic UPD behavior of rechargeable batteries into the limelight.

Keywords: underpotential deposition, Zn metal deposition, zinc-ion battery, aqueous battery, degradation mechanism

1. Introduction

Lithium-ion batteries (LIBs) attract much interest and dominate the marketplace. However, further development of LIBs is hindered by the high cost, flammability, and toxicity problems [1-10]. In recent years, aqueous rechargeable batteries (ARBs) have thrived due to the merits of aqueous electrolytes, including low cost, non-flammable, non-toxicity, and high ionic-conductivity (over 3-orders higher than organic electrolytes) [11-15]. Hence, ARBs are promising for large-scale energy storage and fast charging.

Aqueous zinc-ion batteries (AZIBs) attract much attention owing to the merits of zinc, including high theoretical capacity (820 mAh g^{-1}), abundant source, non-toxicity, and the relatively low redox potential (-0.76 V *vs.* standard hydrogen electrode (SHE)) [16-24]. Therein, cathode materials including manganese-based oxide [25,26], vanadium-based compounds [27,28], Prussian blue analogues [29,30], and organic compounds [31], have been extensively investigated. It is found that Zn^{2+}/H^+ co-uptake mechanisms exist widely in various cathode materials, for example, Liu and co-workers reported an α-MnO_2 cathode for AZIBs and revealed that the chemical conversion reaction between α-MnO_2 and H^+ was mainly responsible for the good performance [32], in the meantime, the product of $ZnSO_4[Zn(OH)_2]_3 \cdot xH_2O$ was detected. Zheng and co-workers reported that Zn^{2+}/H^+ co-insertion kept the interlayer spacing of $Zn_{0.3}V_2O_5 \cdot 1.5H_2O$ cathode constant [33], leading to high capacity and long-term cycling stability. The H^+ insertion would be accompanied by a concentration increase of surface OH^-, which results in the formation of $Zn_x(OTf)_y(OH)_{2x-y} \cdot nH_2O$ ($OTf=CF_3SO_3$). Kundu and co-workers found that the $Zn_4SO_4(OH)_6 \cdot 5H_2O$ and (OTf^-)-based layered double hydroxide (Zn-LDH) deriving from H^+ insertion can promote H^+ insertion, which increased the specific capacity [34]. It seems that the Zn^{2+}/H^+ co-insertion and the accompanied Zn-LDH can help construct better cathode materials.

Nevertheless, we notice that the above-mentioned Zn-LDH exists throughout the whole reaction,

which just indicates the Zn-LDH forms irreversibly and would accumulate as the reaction goes on. The irreversible reaction would consume electrolyte and cause capacity fading, especially at low current densities (which usually correspond to high capacities) [35-37], similar to solid–electrolyte interphase (SEI) or cathode–electrolyte interphase (CEI) in LIBs [38,39]. More importantly, the newly formed Zn-LDH changes potential distribution and solvent molecular orientation at the cathode-electrolyte interface significantly, leading to the possibility of underpotential deposition (UPD) of zinc on the Zn-LDH. The UPD usually occurs when a metal ion forms an adsorbed layer on the surface of another metal at a much higher redox potential than its SHE potential, which was classified by Dunn and co-workers as one of the three typical pseudocapacitance mechanisms in 2014 [40]. However, from then on, few research regarding cathodic UPD in rechargeable batteries can be found, and the metal deposition well above 0 V (*vs.* its SHE potential) was overlooked.

Here, we discovered unusual Zn deposition on the cathode at a potential much higher than the standard Zn deposition potential. Detailed experimental investigations show that the $Zn_x(OTf)_y(OH)_{2x-y}\cdot nH_2O$ originating from H^+ insertion serves as the matrix for the Zn deposition. It is verified that the Zn deposition follows a two-dimensional nucleation and growth model, manifesting a UPD process of zinc metal. Theoretically, the UPD reaction is proved thermodynamically feasible through DFT calculations. The process is observed highly irreversible along with the severe accumulation of Zn metal, leading to inferior cycling stability. By controlling the end-of-discharge voltage to avoid Zn deposition, the reversibility and cyclic performance of the battery can be significantly improved. This finding provides new insights into the degradation of AZIBs and brings cathodic UPD of metal ions into the study of rechargeable batteries.

2. Results and discussion

2.1 Identification of cathodic Zn UPD

VO_2, as a typical cathode material for AZIBs, was used as a model to study the evolution of Zn-LDH upon the cathode material during Zn^{2+}/H^+ storage. The zinc-ion coin cells were fabricated using VO_2 (Fig. S1) as the cathode, zinc foil as the anode, and aqueous 3M $Zn(OTf)_2$ as the electrolyte. As shown in the cycling performance test at a current density of 2 A g^{-1}, the capacity decays 0.2% in each cycle (Fig. S2). Similar poor cyclic performance under deep charge/discharge conditions (corresponding to relatively high capacity) was widely observed in previous works [41]. To understand this phenomenon, we detailly investigated the electrochemical reactions during the fast capacity fading.

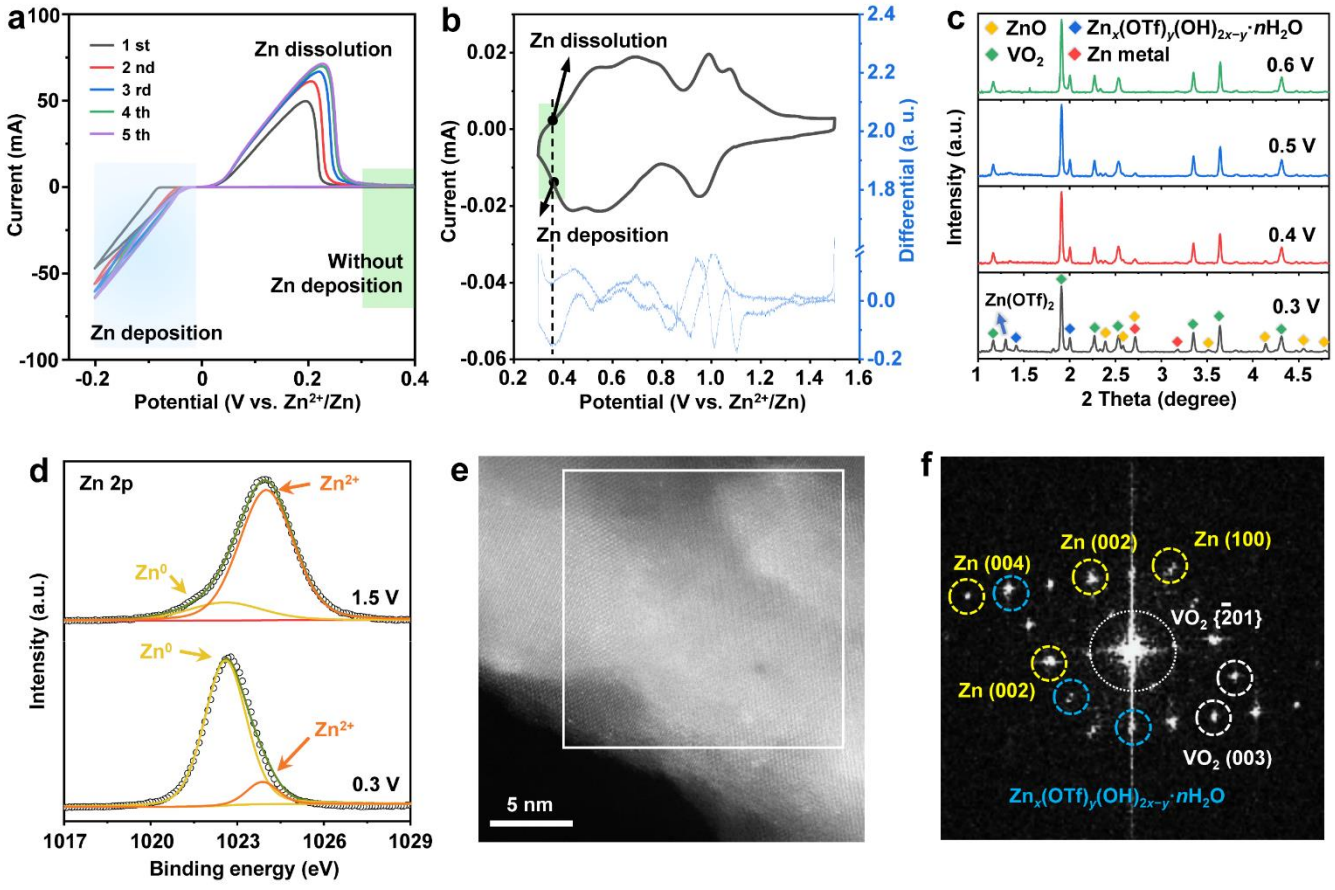

Fig. 1. Identification of cathodic Zn UPD and detection of Zn metal on the cathode after cycling between 0.3 and 1.5 V. (a) Cyclic voltammograms of Zn-Zn symmetric cell at potential scanning rate of 0.5 mV s^{-1}. (b) Cyclic voltammogram (black line) and its differential curve (blue line) of the VO_2//Zn system at 0.1 mV s^{-1} during the initial reversible cycle. (c and d) *Ex situ* characterizations of the VO_2 cathode during the first discharge/charge process, including (c)

HEXRD patterns and (d) XPS spectra. (e) HAADF-STEM image of the VO_2 cathode in the discharged state. (f) Corresponding Fourier transform of (e).

As shown in Fig. 1a, we assembled Zn-Zn symmetric cell with 3 M $Zn(OTf)_2$ aqueous solutions and observed reversible electrochemical deposition/dissolution of Zn. Therein, Zn deposition occurs between -0.2 to 0 V and no peaks of Zn deposition appeared between 0.3 to 0.4 V. Using the same 3 M $Zn(OTf)_2$ solution, we assembled a VO_2//Zn battery. By differentiating the CV curves of the VO_2//Zn battery, we discovered a pair of sharp peaks at about 0.35 V (Fig. 1b). In order to figure out where these two peaks stem from, we performed synchrotron high-energy X-ray diffraction (HEXRD) investigations towards VO_2 cathode (Fig. 1c). We observed the appearance of Zn metal between 0.4 and 0.3 V during first discharge. To the best of our knowledge, this is the first time that Zn metal is observed on cathode materials after cycles. The detection of ZnO can be attributed to the oxidation of nanocrystalline Zn metal with the dissolved O_2 in the electrolyte [42].

Besides, we also observed the formation of $Zn_x(OTf)_y(OH)_{2x-y}\cdot nH_2O$ (Fig. 1c and S3). According to previous reports, along with H^+ insertion into the active materials, the remaining OH^- on the cathode surface would react with Zn^{2+}, H_2O, and $Zn(OTf)_2$ to form $Zn_x(OTf)_y(OH)_{2x-y}\cdot nH_2O$ precipitation [33]. Further, we carried out XPS analysis and deconvolved the Zn 2p peak (Fig. 1d). The remarkable presence of the low-binding-energy (1022.8 eV) peak can be designated to Zn^0 (Zn metal) at 0.3 V, and this is consistent with the energy disperse spectroscopy (EDS) mappings and corresponding energy dispersive X-ray (EDX) patterns (Fig. S4) showing that the Zn signals are stronger than V (which indicate there are Zn monomers). Combined with the high-angle annular dark-field-scanning transmission electron microscopy (HAADF-STEM) image and its Fourier transform pattern (Fig. 1e and 1f), we confirmed the formation of Zn metal at 0.3 V. To exclude the possibility of Zn metal shuttling from anode to the cathode in a coin cell, we also assembled a two-electrode cell with a distance between anode and cathode ca. 2 cm and still detected Zn metal at 0.3 V (Fig. S5). Thus, the peaks at about 0.35

V in Fig. 1b can be related to the Zn deposition/dissolution process, which contradicts Fig. 1a.

2.2 Effects of cathodic Zn UPD

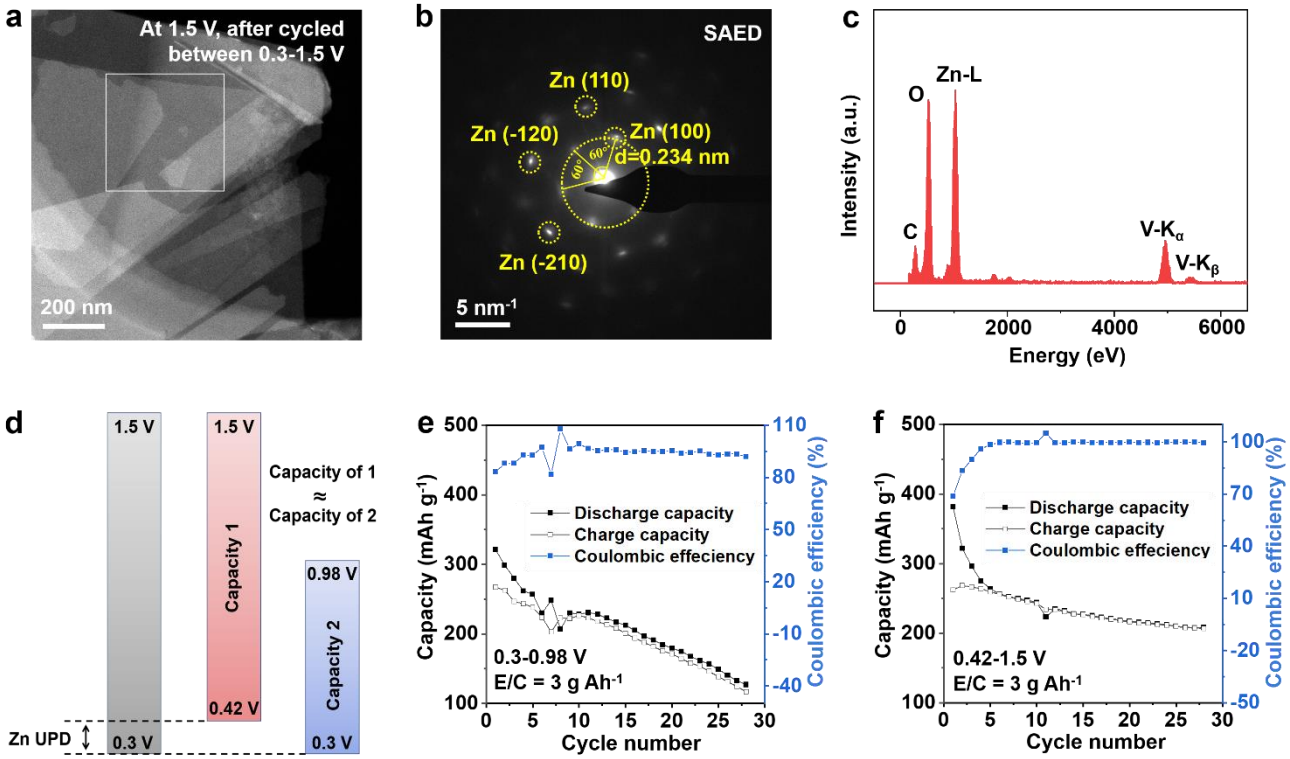

Fig. 2. Effects of cathodic Zn UPD and characterizations and electrochemical tests of the VO_2 cathode within different voltage windows. (a-c) The VO_2//Zn battery operates between 0.3 and 1.5 V. (a) HAADF-STEM image, (b) SAED pattern, and (c) EDX spectrum, recorded at 1.5 V after 50 cycles. (d) Schematic of two artificially set voltage windows with and without Zn UPD. The two sets show similar capacities and charge/discharge depth. (e,f) Cycling performance at an E/C ratio of 3.0 g Ah^{-1} in the voltage windows of (e) 0.3 to 0.98 V and (f) 0.42 to 1.5 V.

After 50 cycles at 1.5 V, we observed a large Zn sheet lying on the carbon grid (Fig. 2a and S6). Fig. 2b is the selected area electron diffraction (SAED) image collected from the white frame in Fig. 2a. According to PDF card of Zn, the crystal system of Zn belongs to hexagonal system. By measuring angle and calculating distance between the diffraction pattern and the central bright spot, the interplanar spacing and crystal plane can be confirmed which are agreement with crystal plane of Zn (110), (110),

(-120) and (-210). As shown in Fig. 2c, the Zn signal is stronger than the other elements, indicating the existence of Zn metal. The occurrence of Zn metal at 1.5 V indicates its irreversibility during cycling, which was also demonstrated in the *ex situ* XRD patterns of different cycles where the accumulation of Zn metal in the full charged state was observed (Fig. S7). The irreversible formation of Zn metal may consume a lot of electrolytes and is detrimental for battery's cycle lifespan [43].

To figure out the relationship between the cathodic Zn metal deposition and the fast capacity fading (mentioned in Fig. S2), we considered avoiding the cathodic Zn deposition whilst minimizing capacity loss. Consequently, staircase potential electrochemical impedance spectroscopy (SPEIS) was performed to investigate the onset potential of Zn metal deposition (Fig. S8). We found that a new interface appeared between 0.417 and 0.397 V in the Nyquist plot and the corresponding Bode plot during the first discharging, which could be attributed to the newly formed phase of Zn metal. Hence, we set a new voltage window of 0.42-1.5 V for the VO_2//Zn system, and we set another voltage window of 0.3-0.98 V that shows similar capacity to the 0.42-1.5 V as contrast (Fig. 2d and S9). In order to amplify the difference, we reduce the amount of electrolyte to a realistic condition (the electrolyte to cathode capacity ratio (i.e. E/C ratio) is 3.0 g Ah^{-1}) [44]. It can be clearly observed that coulombic efficiency (CE) is ~90% when cycling between 0.3-0.98 V (Fig. 2e) and is ~100% when cycling between 0.42-1.5 V (Fig. 2f), meanwhile, cycling stability of the latter is much better than the former one.

Ex situ EIS was employed to give further insight. As can be seen in the Nyquist plot and the corresponding Bode plot of the pristine sample, there are two semicircles at high-frequency region (Fig. S10a and S10b), indicating there are two reaction interfaces at the pristine state. To investigate the origin of the second phase in its pristine state, the pristine VO_2 was soaked in the electrolyte for 3h. After soaking, $Zn_x(OTf)_y(OH)_{2x-y}\cdot nH_2O$ was formed (Fig. S11), suggesting that H^+ would be

spontaneously absorbed into VO_2 and the second phase of $Zn_x(OTf)_y(OH)_{2x-y}\cdot nH_2O$ would be generated in the pristine state. After being cycled for two times in the voltage window of 0.3 to 1.5 V, the third semicircle appeared at 1.5 V (Fig. S10c-f), which became more obvious after being cycled for three times (Fig. 3a and 3b), corresponding to the formation of Zn metal and its accumulation. On the other hand, after being cycled for three times in the voltage window of 0.42 to 1.5 V, there was only one semicircle in the Nyquist plot and Bode plot (Fig. 3c and 3d), indicating the elimination of the irreversible formation of Zn metal and $Zn_x(OTf)_y(OH)_{2x-y}\cdot nH_2O$. Comparing the above two voltage windows, we revealed that the irreversible Zn metal deposition would cause severe battery degradation, which can be avoided by controlling the end-of-discharge voltage with only a small fraction (~4%) of their energy density sacrificed (Fig. S12).

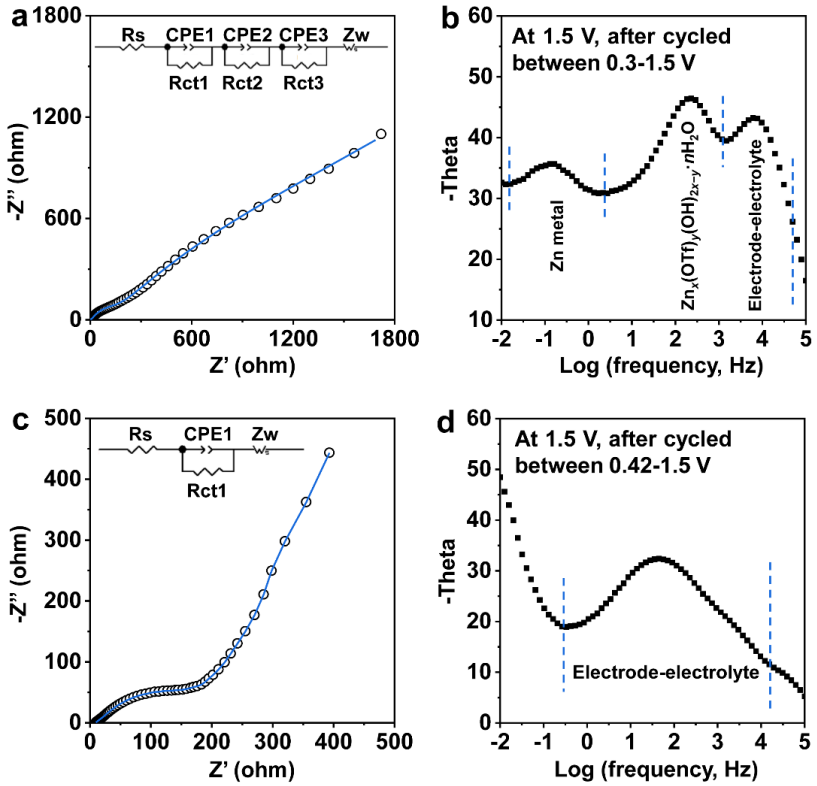

Fig. 3. Removal of cathodic Zn UPD by controlling the end-of-discharge voltage. (a,b) EIS test recorded at 1.5 V after 3 cycles in the voltage window of 0.3 to 1.5 V. (a) Nyquist plot and (b) corresponding Bode plot. (c,d) EIS test recorded at 1.5 V after 3 cycles in the voltage window of 0.42 to 1.5 V. (c) Nyquist plot and (d) corresponding Bode plot.

2.3 Analysis of matrix for Zn UPD

As seen from Fig. 1f and 2b, Zn metal seems to appear where there is $Zn_x(OTf)_y(OH)_{2x-y}\cdot nH_2O$ originating from H^+ insertion. By performing fast Fourier transforms towards the atomic-level HAADF-STEM images (Figs. 4a, 4b and S13), we can clearly observe that Zn metal is distributed in the presence of $Zn_x(OTf)_y(OH)_{2x-y}\cdot nH_2O$. Electron energy loss spectroscopy (EELS) investigations were also carried out. From Fig. 4c and 4d, the Zn metal is enriched where both V and O are sparse, suggesting that cathodic Zn deposition sites are not dependent on VO_2. Combined with the above analysis, Zn is deposited on $Zn_x(OTf)_y(OH)_{2x-y}\cdot nH_2O$ rather than VO_2, as schematically illustrated in Fig. 4e and 4f.

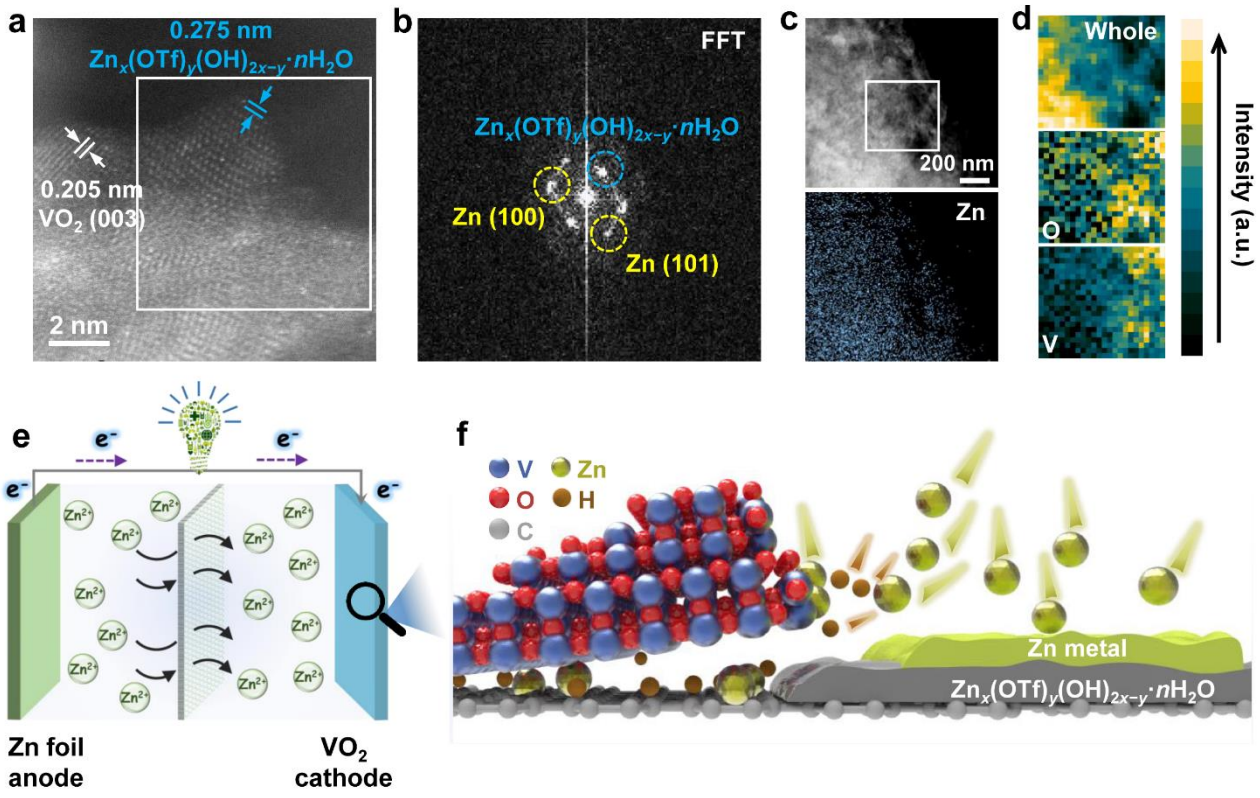

Fig. 4. Investigation of the form of cathodic Zn deposition. (a and b) HAADF-STEM images and corresponding Fourier transform at 0.3 V. (c) HAADF-STEM image and corresponding EDS mapping of Zn element. (d) EELS mapping collected from the white box in (c). (e) Operation schematic of the VO_2//Zn battery. (f) Schematic illustration of Zn^{2+}/H^+ insertion and Zn UPD on the VO_2 cathode.

2.4 Simulations of the Zn UDP

To gain further insight into the formation process of Zn metal, we analyzed in detail the multi-sweep rate CV curves of the VO_2//Zn system. The CV curves with sweep rates ranging from 0.1 to 200 mV s^{-1} were presented in Fig. S14. Based on the two-dimensional phase transitions model proposed by Camacho and co-workers [45], the peak at 0.35 V was studied by differentiating the curve at each sweep rate. From Fig. 5a, we obtained a good linear relationship between the peak current (i_p) and $v^{2/3}$ with a slope of 0.00682. By further fitting lgi_p with lg$v$ and lgΔE_p with lg$v$ (Fig. 5b and 5c), the linear slopes were calculated to be 0.598 and 0.46, respectively, close to the theoretical values of 0.6 and 0.4 in Camacho's model. Therefore, the formation of Zn metal on $Zn_x(OTf)_y(OH)_{2x-y}\cdot nH_2O$ follows the two-dimensional nucleation and growth model, corresponding to the Zn UPD process. Furthermore, this phenomenon is analogous with the UPD of Zn on Ni [46], Pt, Pd and Au electrodes [47], which show underpotential shifts of about 0.6 V, 1.1 V, 1.1 V, and 0.6-0.7 V, respectively.

Density functional theory (DFT) calculations were performed to measure the thermodynamic possibility of Zn UPD on $Zn_x(OTf)_y(OH)_{2x-y}\cdot nH_2O$. It was reported that the UPD occurs only in the case that the metal with a smaller work function deposits on the metal with a larger work function [48]. Thereby, we carried out three kinds of algorithms of GGA-PBE, mGGA-M06L (Fig. S15), and LDA-PWC (Fig. 5d and 5e) to evaluate the work functions of Zn metal and $Zn_x(OTf)_y(OH)_{2x-y}\cdot nH_2O$. The work function values of $Zn_x(OTf)_y(OH)_{2x-y}\cdot nH_2O$ obtained from mGGA-M06L and LDA-PWC algorithms were close to each other, while LDA-PWC exhibited a closer value of Zn metal compared to its experimental result. Therefore, the work function of Zn metal and $Zn_x(OTf)_y(OH)_{2x-y}\cdot nH_2O$ were determined to be 0.157 Ha and 0.292 Ha, respectively, by the LDA-PWC algorithm. As a result, the much larger work function of $Zn_x(OTf)_y(OH)_{2x-y}\cdot nH_2O$ than Zn metal would facilitate the underpotential deposition reaction.

Beyond the discovery of Zn UPD in the VO_2//Zn system, we also observed it in TiO_2 (Figs. S16

and S17) and SnO_2 (Figs. S18 and S19) cathodes for AZIBs, indicating the universal presence of Zn UPD in different AZIBs.

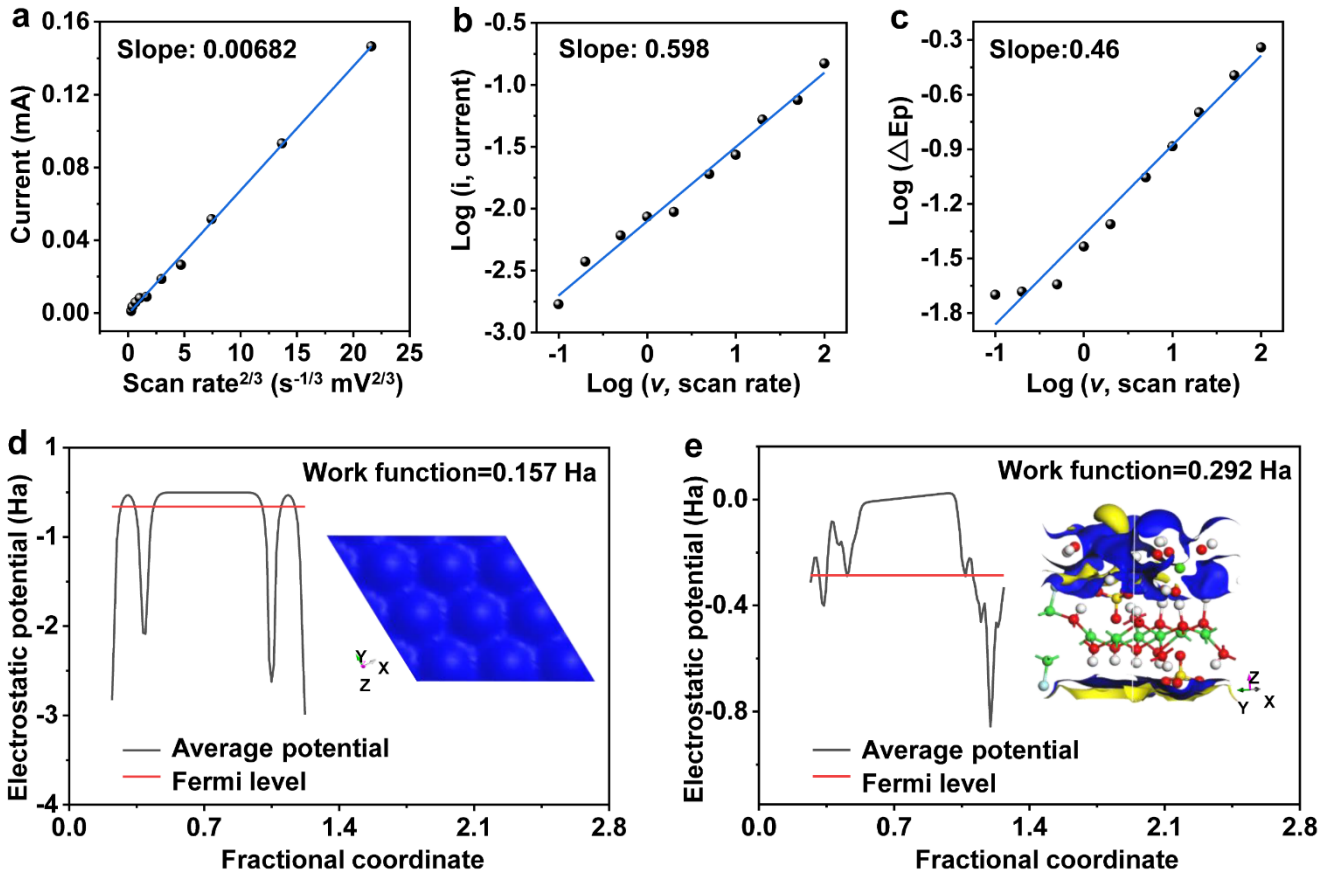

Fig. 5. Electrochemical fitting and theoretical calculation of the Zn UDP. (a-c) Fitting of the multi-sweep rate CV curves ranging from 0.1-100 mV s^{-1}. Plots of (a) i_p with $v^{2/3}$, (b) lgi_p with lg$v$, and (c) lgΔEp with lg$v$. (d,e) DFT calculations with LDA-PWC algorithm for calculating the work functions of (d) Zn metal and (e) $Zn_x(OTf)_y(OH)_{2x-y}\cdot nH_2O$. The insets in (d) and (e) are the calculated surface of Zn and $Zn_x(OTf)_y(OH)_{2x-y}\cdot nH_2O$, respectively.

3. Conclusion

In conclusion, we uncover the Zn UPD on the VO_2 cathode through *ex situ* HAADF-STEM, *ex situ* HEXRD, *ex situ* EIS, SPEIS and *ex situ* XPS investigations. The $Zn_x(OTf)_y(OH)_{2x-y}\cdot nH_2O$ originating from H^+ insertion is the deposition matrix, and we confirm that the Zn UPD follows a two-dimensional nucleation and growth model by detailly fitting its CV peaks. We have also verified the thermodynamic feasibility of the UPD process by means of DFT calculations. Moreover, we observe the accumulation

of Zn metal after cycling, indicating this UPD reaction is irreversible and harmful for the cycling stability of AZIBs. By increasing the end-of-discharge voltage slightly from 0.3 V to 0.42 V, the Zn UPD is significantly mitigated, and the cycling stability of the battery is effectively improved. The low-potential Zn UPD reveals a new mechanism of the degradation of AZIBs, which can be avoided by not discharging to too low a potential. More importantly, this discovery will contribute to further research and application of cathodic UPD, as the UPD is a typical pseudocapacitive reaction mechanism that can exhibit high charge/discharge rates.

4. Experimental section

4.1 Synthesis of VO_2 electrode

Typically, 150 mg of V_2O_5 and 26 mg of rGO were added to n-propanol to form a 30 mL mixture solution. The mixture was then transferred into a 50 mL Teflon-lined autoclave and heated at 180 °C for 12 h. After naturally cooling to room temperature, we obtained the blue precipitates. Afterward, the precipitates were washed with ethyl alcohol and deionized water several times, respectively, and then dispersed into an aqueous solution. Next, we added the single-walled carbon nanotubes into the solution and mixed them homogenously. Finally, the above mixture solution was filtrated under a vacuum into a VO_2 film electrode.

4.2 Material Characterization

The morphologies, crystallographic and microstructural characteristics of the samples were measured using field emission scanning electron microscopy (FE-SEM, JEOL-7100F), scanning transmission electron microscopy (STEM, Titans Themis, the tests were carried based on samples lying on carbon grids), selected area electron diffraction (SAED), energy dispersive spectrometer (EDS), energy dispersive X-ray (EDX), X-ray diffraction (XRD, D8 Advance X-ray diffractometer with a Cu Kα radiation source) and synchrotron high-energy X-ray diffraction (HEXRD, at beamline 11-ID-C of

Advanced Photon Source (APS) at Argonne National Laboratory; a beam with a size of 0.2 mm × 0.2 mm and wavelength of 0.1173 Å was used to obtain diffraction patterns). The chemical states and atomic structure information were investigated by X-ray photoelectron spectroscopy (XPS, Thermo Fisher Scientific- ESCALAB 250Xi).

4.3 Electrochemical Measurements

The mass loading of the VO_2 film cathode is about 2.3 mg cm^{-2}. CR2016 coin cells were assembled for measuring the electrochemical performance of the VO_2 film. Besides, commercial glass fiber and zinc foil were employed as the separator and anode, respectively. Aqueous 3M $Zn(OTf)_2$ solution was used as the electrolyte. The galvanostatic charge/discharge (GCD) tests were performed on a battery test system (LAND CT2001A). CV and EIS were measured using an electrochemical workstation (EC-LAB, VMP-3, Bio-Logic SAS). The two-electrode test was performed with a distance between anode and cathode ca. 2 cm on an electrochemical workstation (CHI760E).

Declaration of Competing Interest

The authors declare that they have no known competing financial interests or personal relationships that could have appeared to influence the work reported in this paper.

Acknowledgements

This work was supported by the National Key Research and Development Program of China (2020YFA0715000 and 2016YFA0202603) and the National Natural Science Foundation of China (51832004, 51521001, and 22109029).

Appendix A. Supplementary data

Supplementary data associated with this article can be found in the online version.

References

[1] Dunn B, Kamath H, Tarascon JM. Electrical energy storage for the grid: A battery of choices. Science 2011; 334: 928-935.

[2] Nam KW, Kim H, Beldjoudi Y, et al. Redox-active phenanthrenequinone triangles in aqueous rechargeable zinc batteries. J Am Chem Soc 2020; 142: 2541-2548.

[3] Li W, Dahn JR, Wainwright DS. Rechargeable lithium batteries with aqueous electrolytes. Science 1994; 264: 1115-1118.

[4] Luo JY, Cui WJ, He P, et al. Raising the cycling stability of aqueous lithium-ion batteries by eliminating oxygen in the electrolyte. Nat Chem 2010; 2: 760-765.

[5] Yang C, Chen J, Ji X, et al. Aqueous Li-ion battery enabled by halogen conversion-intercalation chemistry in graphite. Nature 2019; 569: 245-250.

[6] Zhu SH, Chen C, He P, et al. Novel hollow $Ni_{0.33}Co_{0.67}Se$ nanoprisms for high capacity lithium storage. Nano Res 2019; 12: 1371-1374.

[7] Zong W, Guo H, Ouyang Y, et al. Topochemistry-Driven Synthesis of Transition-Metal Selenides with Weakened Van Der Waals Force to Enable 3D-Printed Na-Ion Hybrid Capacitors. Adv Funct Mater 2022; 32: 2110016.

[8] Yang X, Zheng X, Li H, et al. Non-Noble-Metal Catalyst and Zn/Graphene Film for Low-Cost and Ultra-Long-Durability Solid-State Zn-Air Batteries in Harsh Electrolytes. Adv Funct Mater 2022; 2200397.

[9] Zhang W, Wu Y, Xu Z, et al. Rationally Designed Sodium Chromium Vanadium Phosphate Cathodes with Multi-Electron Reaction for Fast-Charging Sodium-Ion Batteries. Adv Energy Mater 2022; 12: 2201065.

[10] Li H, Zhang W, Sun K, et al. Manganese-based materials for rechargeable batteries beyond lithium-ion. Adv Energy Mater 2021; 11: 2100867.

[11] Liu YY, Lu X, Lai FL, et al. Rechargeable aqueous Zn-based energy storage devices. Joule 2021; 5: 2845-2903.

[12] Dai Y, Liao X, Yu R, et al. Quicker and more Zn^{2+} storage predominantly from the interface. Adv Mater 2021; 33: 2100359.

[13] Ding J, Du Z, Gu L, et al. Ultrafast Zn^{2+} intercalation and deintercalation in vanadium dioxide. Adv Mater 2018; 30: 1800762.

[14] Li J, McColl K, Lu X, et al. Multi-scale investigations of δ-$Ni_{0.25}V_2O_5{\cdot}nH_2O$ cathode materials in aqueous zinc-ion batteries. Adv Energy Mater 2020; 10: 2000058.

[15] Chen H, Dai C, Xiao F, et al. Reunderstanding the Reaction Mechanism of Aqueous Zn–Mn Batteries with Sulfate Electrolytes: Role of the Zinc Sulfate Hydroxide. Adv Mater 2022; 34: 2109092.

[16] Chao D, Zhou W, Ye C, et al. An electrolytic Zn-MnO_2 battery for high-voltage and scalable energy storage. Angew Chem Int Ed 2019; 58: 7823-7828.

[17] Yan M, He P, Chen Y, et al. Water-lubricated intercalation in $V_2O_5{\cdot}nH_2O$ for high-capacity and high-rate aqueous rechargeable zinc batteries. Adv Mater 2018; 30: 1703725.

[18] Chao DL, Qiao SZ. Toward high-voltage aqueous batteries: Super-or low-concentrated electrolyte?

Joule 2020; 4: 1846-1851.
[19] Yang W, Du X, Zhao J, et al. Hydrated eutectic electrolytes with ligand-oriented solvation shells for long-cycling zinc-organic batteries. Joule 2020; 4: 1557-1574.
[20] Qiu H, Du X, Zhao J, et al. Zinc anode-compatible in-situ solid electrolyte interphase via cation solvation modulation. Nat Commun 2019; 10: 1-12.
[21] Li Q, Chen A, Wang D, et al. “Soft shorts” hidden in zinc metal anode research. Joule 2022; 6: 273-279.
[22] Li Q, Wang DH, Yan BX, et al. Dendrite issues for zinc anodes in a flexible cell configuration for zinc-based wearable energy-storage devices. Angew Chem Int Ed 2022; 61: e202202780.
[23] Li X, Li M, Luo K, et al. Lattice matching and halogen regulation for synergistically induced uniform zinc electrodeposition by halogenated Ti_3C_2 mxenes. ACS Nano 2021; 16: 813-822.
[24] Cui J, Liu X, Xie Y, et al. Improved electrochemical reversibility of Zn plating/stripping: a promising approach to suppress water-induced issues through the formation of H-bonding. Mater Today Energy 2020; 18: 100563.
[25] Wang D, Wang L, Liang G, et al. A superior δ-MnO_2 cathode and a self-healing Zn-δ-MnO_2 battery. ACS Nano 2019; 13: 10643-10652.
[26] Zhang N, Cheng F, Liu J, et al. Rechargeable aqueous zinc-manganese dioxide batteries with high energy and power densities. Nat Commun 2017; 8: 405.
[27] Dai Y, Li J, Chen L, et al. Generating H^+ in catholyte and OH^- in anolyte: an approach to improve the stability of aqueous zinc-ion batteries. ACS Energy Lett 2021; 6: 684-686.
[28] Kundu D, Adams BD, Duffort V, et al. A high-capacity and long-life aqueous rechargeable zinc battery using a metal oxide intercalation cathode. Nat Energy 2016; 1: 16119.
[29] Liu Z, Pulletikurthi G, Endres F. A prussian blue/zinc secondary battery with a bio-ionic liquid-water mixture as electrolyte. ACS Appl Mater Interfaces 2016; 8: 12158-12164.
[30] Zhang LY, Chen L, Zhou XF, et al. Towards high-voltage aqueous metal-ion batteries beyond 1.5 V: The zinc/zinc hexacyanoferrate system. Adv Energy Mater 2015; 5: 1400930.
[31] Zhao Q, Huang WW, Luo ZQ, et al. High-capacity aqueous zinc batteries using sustainable quinone electrodes. Sci Adv 2018; 4: eaao1761.
[32] Pan HL, Shao YY, Yan PF, et al. Reversible aqueous zinc/manganese oxide energy storage from conversion reactions. Nat Energy 2016; 1: 16039.
[33] Wang L, Huang KW, Chen J, et al. Ultralong cycle stability of aqueous zinc-ion batteries with zinc vanadium oxide cathodes. Sci Adv 2019; 5: eaax4279.
[34] Oberholzer P, Tervoort E, Bouzid A, et al. Oxide versus nonoxide cathode materials for aqueous Zn batteries: an insight into the charge storage mechanism and consequences thereof. ACS Appl Mater Interfaces 2019; 11: 674-682.
[35] Blanc LE, Kundu D, Nazar LF. Scientific challenges for the implementation of Zn-ion batteries.

Joule 2020; 4: 771-799.
[36] Li Z, Ren Y, Mo L, et al. Impacts of oxygen vacancies on zinc ion intercalation in VO_2. ACS Nano 2020; 14: 5581-5589.
[37] Zhu KY, Wu T, Sun SC, et al. Synergistic H^+/Zn^{2+} dual ion insertion mechanism in high-capacity and ultra-stable hydrated VO_2 cathode for aqueous Zn-ion batteries. Energy Storage Mater 2020; 29: 60-70.
[38] Gao Y, Yan Z, Gray JL, et al. Polymer-inorganic solid-electrolyte interphase for stable lithium metal batteries under lean electrolyte conditions. Nat Mater 2019; 18: 384-389.
[39] Liang JY, Zhang XD, Zeng XX, et al. Enabling a durable electrochemical interface via an artificial amorphous cathode electrolyte interphase for hybrid solid/liquid lithium-metal batteries. Angew Chem Int Ed 2020; 59: 6585-6589.
[40] Augustyn V, Simon P, Dunn B. Pseudocapacitive oxide materials for high-rate electrochemical energy storage. Energy Environ Sci 2014; 7: 1597-1614.
[41] Chen L, Ruan Y, Zhang G, et al. Ultrastable and high-performance Zn/VO_2 battery based on a reversible single-phase reaction. Chem Mater 2019; 31: 699-706.
[42] Kundu D, Vajargah SH, Wan LW, et al. Aqueous vs. nonaqueous Zn-ion batteries: consequences of the desolvation penalty at the interface. Energy Environ Sci 2018; 11: 881-892.
[43] Zhang N, Cheng F, Liu Y, et al. Cation-deficient spinel $ZnMn_2O_4$ cathode in $Zn(CF_3SO_3)_2$ electrolyte for rechargeable aqueous Zn-ion battery. J Am Chem Soc 2016; 138: 12894-12901.
[44] Niu C, Pan H, Xu W, et al. Self-smoothing anode for achieving high-energy lithium metal batteries under realistic conditions. Nat Nanotechnol 2019; 14: 594-601.
[45] Maestre MS, Rodríguez-Amaro R, Muñoz E, et al. Use of cyclic voltammetry for studying two-dimensional phase transitions: Behaviour at low scan rates. J Electroanal Chem 1994; 373: 31-37.
[46] Ballesteros JC, Chaînet E, Ozil P, et al. Electrochemical studies of Zn underpotential/overpotential deposition on a nickel electrode from non-cyanide alkaline solution containing glycine. Electrochim Acta 2011; 56: 5443-5451.
[47] Nakamura M, Aramata A, Yamagishi A, et al. Underpotential deposition of zinc ions on Au (111) in phosphate solution (pH 4.6): kinetic and STM studies. Journal of Electroanalytical Chemistry 1998; 446: 227-231.
[48] Leiva E. Recent developments in the theory of metal upd. Electrochimica Acta 1996; 41: 2185-2206.